

# Impact of Sea Spray on Air–Sea Fluxes. Part I: Results from Stochastic Simulations of Sea Spray Drops over the Ocean

JAMES A. MUELLER AND FABRICE VERON

*School of Marine Science and Policy, University of Delaware, Newark, Delaware*

(Manuscript received 1 November 2013, in final form 12 July 2014)

## ABSTRACT

The contributions of sea spray drops to the total air–sea exchanges of momentum, heat, and mass remain an open question. A number of factors obscure any simple quantification of their contribution; the per drop contribution to the fluxes is a particularly important factor that cannot be calculated easily, as are the number of drops formed. To estimate the per droplet fluxes, the authors first calculate the low order statistics from a large number of drop trajectories, which are simulated with a recently developed Lagrangian stochastic model adapted for the heavy drop transport and evaporation within the marine boundary layer. This paper describes the results from simulations of sea spray drops over the ocean, and as one of two parts, summarizes new estimations for the spray-mediated fluxes on a per drop basis. The results suggest that common simplifications in previous sea spray models, such as the residence time in the marine boundary layer, may not be appropriate.

## 1. Introduction

The transfers of momentum, gas, heat, and mass between the atmosphere and the ocean are crucial to the determination and prediction of weather, climate, and the general circulation of both the atmosphere and the ocean. The interaction between the atmosphere and ocean becomes even more complex when the turbulence at the interface is such that the surface itself is multiply connected through the presence of drops and bubbles (Brocchini and Peregrine 2001), leading to multiple boundaries and difficulties in segregating the two fluid phases.

As a component of the air–sea boundary layer, sea spray drops are involved in momentum, heat, water vapor, gas, and other mass transfers with the atmosphere. Spray droplets are formed mainly through two processes. The first, resulting in what are generally called film and jet droplets, occurs when bubbles, previously entrained by breaking waves, rise to the surface and burst, ejecting water droplets into the air. These form with radii on the  $O(1–100)$   $\mu\text{m}$ . The second process occurs when the wind is sufficiently strong to tear off water globules from wave crests. This process generates “spume” drops of radii

$O(20–1000)$   $\mu\text{m}$ . Finally, when water (i.e., rain, sea spray, or breaking waves) impacts the surface, “splash” drops can be formed as well.

Once airborne, sea spray drops scatter radiation and exchange momentum, heat, and moisture with the atmosphere. Some drops will get suspended and evaporate entirely, and others will fall back into the ocean. While suspended in the air, even for a short time, water droplets have time to exchange substantial heat, moisture, and momentum with the atmosphere. Thus, sea spray may carry a significant amount of the total air–sea heat flux under certain conditions. The debate, however, is still open regarding the range of wind speeds over which sea spray effects cannot be neglected (e.g., Lewis and Schwartz 2004, p. 6).

This debate is fueled in part by the large uncertainty in the sea spray source function, that is, the number of drops and their size distribution at a given wind speed. Spume droplets, due to their large relative size, have the potential to transfer considerably more mass, momentum, and heat than jet or film droplets; although the potential is greater, intuition suggests that the residence time of spume droplets will be shorter due to faster settling velocities and to their vastly different ejection mechanism. Therefore, to close the sea spray-mediated momentum, heat, and moisture budgets, one needs a precise knowledge of 1) the droplet physics on a per droplet basis, that is, the air spray fluxes, and 2) the source function.

---

*Corresponding author address:* Fabrice Veron, University of Delaware, 112C Robinson Hall, Newark, DE 19716.  
E-mail: fveron@udel.edu

Edson and Fairall (1994) embarked on a dual component study that is a significant motivation for this present work. Their first part, a Lagrangian model, used the Langevin equation, accounting for inertial effects and assuming Stokes' law (i.e., linear drag force as function of relative velocity) to model the transport of larger droplets. The second part of their study, Edson et al. (1996), was an Eulerian–Lagrangian hybrid model that investigated the interaction of sea spray and the fields of temperature and humidity, but it included neither the effects of the wave field nor the instantaneous thermal evolution of the droplets. The most recent published results of Van Eijk et al. (2001) included the effects of sinusoidal waves but reverted to instantaneous temperature equilibrium for the droplets in the Sea Couche Limite Unidimensionnelle Stationnaire d'Embruns (SEACLUSE) model. Meirink (2002) has since shown the dependence of SEACLUSE on the modeling of airflow over waves. To the authors' knowledge, there has not been a model that included a realistic wave field and simultaneously solved the full equations for the transport and microphysical evolution of spume droplets within a fully turbulent flow.

Before investigating the impact of sea spray, we must first examine the ambient conditions and fluxes at the surface interface and the spray-mediated fluxes on a per drop basis. In section 2, we implement a recent physical model for the interfacial flux components (Mueller and Veron 2009b, 2010a), which incorporates airflow separation over breaking waves and its effects on the other flux components. In section 2, we also succinctly describe a recent Lagrangian stochastic model adapted for heavy particles and drops within the marine boundary layer (Mueller and Veron 2009a, 2010b) to evaluate the spray-mediated fluxes on a per drop basis.

Lagrangian stochastic models can capture the paths of particles (or drops) in the atmospheric boundary layer from knowledge of only the low order statistics of the velocity (Wilson and Sawford 1996). Although less has been reported on the ability of Lagrangian stochastic models to predict the passive scalar evolution of drops, Couzinet (2008) demonstrated fair agreement with direct numerical simulation (DNS) results. Mueller and Veron (2010a) showed that the modeled surface fluxes and mean profiles of velocity, temperature, and humidity fit reasonably well with available experimental data from the Tropical Ocean Global Atmosphere Coupled Ocean–Atmosphere Response Experiment (TOGA COARE; Fairall et al. 1996a, 1997, 2003), the San Clemente Ocean Probing Experiment (SCOPE; Fairall et al. 1996b), Humidity Exchange over the Sea (HEXOS; DeCosmo et al. 1996) experiment, and the Coupled Boundary Layer and Air–Sea Transfer (CBLAST; Drennan et al. 2007; Zhang et al. 2008) experiment. Mueller and Veron (2009a) found

the modeled turbulent stress profiles to be consistent with laboratory experiments showing the rapid distortion of turbulence above wind waves (Mastenbroek et al. 1996) and the DNS results over monochromatic waves from Sullivan et al. (2000). Nevertheless, Lagrangian stochastic models are unable to reproduce large eddies and other large-scale boundary layer structures that are likely to exist in the atmospheric boundary layer (ABL), especially during high wind conditions.

This paper (Part I of II) presents the results from the Lagrangian stochastic model that allow us to evaluate the per droplet spray-mediated fluxes of momentum, sensible, and latent heat. In Mueller and Veron (2014, hereafter referred to as Part II), we are able to evaluate the impact of sea spray on the air–sea fluxes and estimate the total air–sea fluxes under a range of conditions with the results from the Lagrangian stochastic model, Part I, along with two different sea spray generation functions.

## 2. Model description

The bulk parameterization of air–sea fluxes relates measurable variables to the momentum, heat, and water vapor fluxes at the interface:

$$\tau = \rho u_* |u_*| = \rho C_D [U_1(10) - U_1(0)] |U_1(10) - U_1(0)|, \quad (1)$$

$$H = \rho c_p \theta_* |u_*| = \rho c_p C_H [\Theta(10) - \Theta(0)] |U_1(10) - U_1(0)|, \quad (2)$$

$$M = \rho q_* |u_*| = \rho C_E [Q(10) - Q(0)] |U_1(10) - U_1(0)|, \quad (3)$$

where  $U_1(\zeta)$ ,  $\Theta(\zeta)$ , and  $Q(\zeta)$  are, respectively, the mean horizontal wind speed, potential temperature, and specific humidity at height  $\zeta$  and are discussed in more detail below. Also,  $\rho$  and  $c_p$  are the density and isobaric specific heat of moist air, respectively. The transfer coefficients for momentum, heat, and moisture at 10-m height are  $C_D$ ,  $C_H$ , and  $C_E$  and are usually referred to as the drag coefficient, Stanton number, and Dalton number. The respective flux scales for velocity, potential temperature, and specific humidity are  $u_*$ ,  $\theta_*$ , and  $q_*$  and relate to the turbulent fluxes as  $u_* |u_*| = -\overline{u'_1 u'_3}$ ,  $\theta_* |u_*| = -\overline{\theta' u'_3}$ , and  $q_* |u_*| = -\overline{q' u'_3}$ . The primes indicate turbulent quantities; the overbars represent ensemble averages, and the subscripts (1, 2, 3) represent the horizontal long wind, crosswind, and vertical directions, respectively. Note the sign convention in Eqs. (1)–(3), in which positive fluxes are into the ocean and negative fluxes are out of the ocean and into the atmosphere. Finally, the latent

heat flux is  $E = L_v M$ , where  $L_v$  is the latent heat of vaporization.

In the context of this paper, we will consider two distinct pathways through which the ocean and atmosphere interact: the air–sea surface and airborne drops. As many previous studies have suggested (e.g., [Andreas 2011](#), and citations therein), the air–sea interface and air–sea spray interface constitute nearly all of the total air–sea fluxes considered here, so we explicitly assume

$$\tau = \tau_{\text{int}} + \tau_{\text{sp}}, \quad (4)$$

$$H = H_{\text{int}} + H_{\text{sp}} - E_{\text{sp}}, \quad (5)$$

$$E = E_{\text{int}} + E_{\text{sp}}, \quad (6)$$

where the subscripts int and sp denote the air–sea interfacial and spray-mediated components, respectively. The energy necessary to evaporate the droplets must be extracted from the sensible heat in the near-surface atmosphere, and consequently, the spray latent heat flux  $E_{\text{sp}}$  must also appear in the sensible heat flux balance.

#### a. Fluxes at the air–sea interface

Turbulent boundary layer theory over a smooth, flat surface offers a starting point for the mean profiles over ocean waves. Within a classical turbulent boundary layer, two distinct regions exist. The first region, closest to the surface, is the diffusive sublayer, in which molecular effects dominate. The profiles in this layer are linear with distance orthogonal to the boundary. The second region is the log layer, where the turbulent fluxes dominate, and the profiles become logarithmic. In smooth flow, these two regions are self-similar in wall coordinates (i.e., normalized distance from the wall boundary  $z^+ = zu_*/\nu$ , where the flux scale  $u_*$  is also known as the friction velocity and  $\nu$  is the kinematic viscosity of the air). In the atmospheric boundary layer, waves form, grow, interact, and break. The surface moves and becomes hilly and rough. The velocity profile over ocean waves, not surprisingly, departs from the classical boundary layer case, and the changes in the momentum flux also translate to a departure from smooth flow for the scalar fluxes as well ([Mueller and Veron 2010a](#)).

Assuming the profile forms for velocity, temperature, and water vapor [see Eqs. (7)–(9)] as well as the bulk “measurable” conditions at the surface and 10-m height, we first estimate the surface fluxes ( $\tau_{\text{int}}$ ,  $H_{\text{int}}$ , and  $E_{\text{int}}$ ) as those of a classical boundary layer. With an empirical omnidirectional wave spectrum model ([Elfouhaily et al. 1997](#)), we then calculate the wave-induced stress and the stress from airflow separation over breaking waves. We also find the fraction of surface area that is sheltered by

the regions of airflow separation and reduce the viscous stress component from the smooth flow case proportionately. Because the wave model depends on the surface stress, we perform multiple iterations until convergence. The details of the surface stress model can be found in [Mueller and Veron \(2009b\)](#). While the heat and water vapor flux scales ( $\theta_*$  and  $q_*$ ) are assumed to remain unchanged from their values in the smooth flow case, the heat and water vapor fluxes do not remain constant because the momentum flux scale, or friction velocity, changes. The details of the scalar flux model at the surface can be found in [Mueller and Veron \(2010a\)](#).

The form for the mean velocity, temperature, and humidity profiles is determined using a hybrid of the standard logarithmic profile from flat plate theory and the van Driest damping function ([Van Driest 1956](#)), which approximates both the near-wall, linear, molecular sublayer and the smooth transition to the log layer. The mean profiles are simply the summation of the two layers, with the logarithmic layer exponentially damped in the near-wall region. Assuming constant flux layers and using the notation of [Liu et al. \(1979\)](#), we prescribe the mean profiles as given in [Mueller and Veron \(2010a\)](#), with further simplification:

$$U_1(\xi) - U_1(0) = [1 - \exp(-\xi u_*/C\nu)] \times \left\{ C u_{*v} \left| \frac{u_{*v}}{u_*} \right| + \frac{u_*}{k} \left[ \ln \left( \frac{\xi + \delta_m}{\delta_m} \right) - \Psi_m \right] \right\}, \quad (7)$$

$$\Theta(\xi) - \Theta(0) = [1 - \exp(-\xi u_*/S\kappa)] \times \left\{ S \theta_* \left| \frac{u_{*v}}{u_*} \right| + \frac{\theta_*}{k} \left[ \ln \left( \frac{\xi + \delta_\theta}{\delta_\theta} \right) - \Psi_\theta \right] \right\}, \quad (8)$$

$$Q(\xi) - Q(0) = [1 - \exp(-\xi u_*/D\epsilon)] \times \left\{ D q_* \left| \frac{u_{*v}}{u_*} \right| + \frac{q_*}{k} \left[ \ln \left( \frac{\xi + \delta_q}{\delta_q} \right) - \Psi_q \right] \right\}, \quad (9)$$

where  $C$  is the viscous layer height in wall coordinates and is usually taken to be  $O(10)$ . Here,  $k = 0.4$  is the von Kármán constant, and  $\rho u_{*v}^2$  represents the viscous component of the total surface stress  $\rho u_*^2$ . Also,  $\kappa$  and  $\epsilon$  are the molecular diffusivities for heat and water vapor, respectively;  $S$  and  $D$  are the scaled heights of the molecular layers in the corresponding wall coordinates and relate to the viscous sublayer  $C$  with  $S = CPr^{1/2}$  and  $D = CSc^{1/2}$ , where  $Pr = \nu/\kappa$  and  $Sc = \nu/\epsilon$  are, respectively, the Prandtl ( $\approx 0.72$  at  $20^\circ\text{C}$ ) and Schmidt ( $\approx 0.63$  at  $20^\circ\text{C}$ ) numbers. The stability corrections due to stratification

$[\Psi_m(\zeta/L), \Psi_\theta(\zeta/L), \text{ and } \Psi_q(\zeta/L)]$  are a function of the height  $\zeta$  and the Obukhov length scale  $L$ . The variables  $\delta_m$ ,  $\delta_\theta$ , and  $\delta_q$  merely ensure a smooth transition between the two layers, regardless of the flow roughness, and are related to the respective roughness lengths  $z_m$ ,  $z_\theta$ , and  $z_q$  through (Mueller and Veron 2010b)

$$\delta_m = z_m \exp \left[ Ck \left( \frac{u_{*v}}{u_*} \right) \left| \frac{u_{*v}}{u_*} \right| \right], \quad (10)$$

$$\delta_\theta = z_\theta \exp \left( Sk \left| \frac{u_{*v}}{u_*} \right| \right), \quad (11)$$

$$\delta_q = z_q \exp \left( Dk \left| \frac{u_{*v}}{u_*} \right| \right). \quad (12)$$

The profile form given in Eqs. (7)–(9) offers a continuous (and second-order differentiable) formulation that smoothly connects the molecular (linear) and log layers. The profiles converge to the expected limits near the surface and to the standard, nonsingular log layers outside the molecular sublayers. The kinematic molecular fluxes at the surface are also recovered.

Note that for the bulk flux calculations, the vertical coordinate  $\zeta$  is simply the distance above the mean water level. It is a wave-following coordinate in the Lagrangian stochastic model, which will be discussed in detail below [see Mueller and Veron (2009b) for details].

### b. Fluxes at the air spray interface

To estimate the contributions of sea spray to the total air–sea fluxes, there are two classes of relevant questions to address. The first class of questions concerns the exchanges between the drops and the atmosphere: how much momentum, heat, and mass do the drops exchange, on average? How long are the drops in the air? And how many drops stay suspended indefinitely? The second class of questions concerns the production of sea spray: how many drops are produced? And what is their size distribution? To address the first set of questions, which is the primary focus of this paper, we employ a Lagrangian stochastic model of the drops. We discuss the second set of questions in Part II, where we examine the model results considering two different sea spray generation functions.

#### 1) LAGRANGIAN STOCHASTIC MODEL

In addition to the number of drops formed, the average droplet trajectories and fluxes per drop are necessary to estimate the total spray-mediated fluxes. For these calculations, we developed and employed a Lagrangian stochastic model.

To model the instantaneous velocity, temperature, and specific humidity of the airflow in the ABL, above

a wavy surface, we use the standard Reynolds decomposition in which the velocity vector  $\mathbf{u}$ , potential temperature  $\theta$ , and specific humidity  $q$  of the air are represented, respectively, by

$$u_i = U_i + u'_i, \quad (13)$$

$$\theta = \Theta + \theta', \quad (14)$$

$$q = Q + q'. \quad (15)$$

Here,  $U_i$ ,  $\Theta$ , and  $Q$  are the ensemble (or temporal) averages in surface-following coordinates [see Eqs. (7)–(9)];  $u'_i$ ,  $\theta'$ , and  $q'$  are the turbulent deviations from the respective means. In this model, we only consider the streamwise horizontal and vertical directions, that is,  $i = (1, 3)$  and the turbulent velocities contain a wave-coherent component [for details, see Mueller and Veron (2009a)].

#### (i) Deterministic components of the air

The mean profiles are those in Eqs. (7)–(9), but now the vertical coordinate  $\zeta$  is equivalent to the distance above the local surface  $\zeta(x, z, t) = z - \eta(x, t)$ , where  $\eta(x, t)$  is the instantaneous wavy water surface. As the vertical coordinates follow the surface displacement, the mean velocity, temperature, and water vapor profiles are shifted up and down relative to a fixed coordinate system. For bulk conservation of mass, the airflow is accelerated in places where the water level is above the mean water level and decelerated in places where the water level is below the mean water level (Mueller and Veron 2009a, appendix A). The motion of the waves induces an orbital velocity component, and the mere presence of the waves produces local vertical velocities such that the airflow follows the surface. All wave-induced velocities are exponentially damped away from the surface, scaled by the wavenumber.

We choose to follow the empirical omnidirectional spectrum of Elfouhaily et al. (1997) to describe the amplitudes of capillary and deep-water gravity wave modes  $A_n$ , but any other spectrum could be substituted. The instantaneous elevation of the surface is then estimated as a linear superposition of these modes and becomes

$$\eta(x, t) = \sum_n A_n \cos(k_n x - \omega_n t + \varphi_n), \quad (16)$$

where  $k_n$ ,  $\omega_n$ , and  $\varphi_n$  are the wavenumber, orbital frequency, and phase of each wave mode  $n$ , respectively. The phase speed of each mode is determined by the dispersion relationship for deep-water capillary–gravity waves. Each wave phase  $\varphi_n$  is chosen from a random distribution uniformly distributed on the interval  $[-\pi, \pi]$ .

(ii) *Stochastic, turbulent components of the air*

We assume that the velocity of an air parcel evolves as a Markov process in which consecutive values in time are partially correlated, while the uncorrelated component is independent of previous values. We model the remaining stochastic, turbulent component of the velocity by solving for the turbulent component of the generalized Langevin equation, simplified with appropriate assumptions for the ABL.

The generalized Langevin equation is (Thomson 1987)

$$du_i = a_i dt + b_{ij} d\xi_j, \quad (17)$$

where  $d\xi_j$  is an independent Gaussian variable with zero mean and variance  $dt$ ; here,  $b_{ij} = \sqrt{C_0 \epsilon_m \delta_{ij}}$  with the Kolmogorov constant from the second-order Lagrangian structure function in the inertial subrange  $C_0$  and the mean rate of kinetic energy dissipation  $\epsilon_m$  (see Mueller and Veron 2009a). The usual summation convention on repeated indices applies. When  $a_i = -u_i/T_L$ , the classical Langevin equation is recovered with the Lagrangian velocity integral time scale  $T_L$ . The classical Langevin equation does not strictly apply to inhomogeneous or nonstationary flows, however. Thomson (1987) pointed out that the classical Langevin equation fails to satisfy what he called the ‘‘well-mixed criterion,’’ which requires a passive tracer that is initially well mixed to stay well mixed. Yet, the imposition of the well-mixed criterion does not yield a unique solution for  $a_i$  in multiple dimensions (Thomson 1987).

Thomson’s (1987) simplest solution to the well-mixed criterion, in tensor notation with usual summation convention, is

$$a_i = -\frac{C_0 \epsilon_m \hat{\tau}_{ik}^{-1} u'_k}{2} + \phi_i, \quad (18)$$

and

$$\begin{aligned} \phi_i = & \frac{\partial U_i}{\partial t} + U_j \frac{\partial U_i}{\partial x_j} + \frac{1}{2} \frac{\partial \hat{\tau}_{ij}}{\partial x_j} + \frac{\hat{\tau}_{im}^{-1}}{2} \frac{\partial \hat{\tau}_{km}}{\partial x_j} u'_j u'_k \\ & + \left[ \frac{\partial U_i}{\partial x_j} + \frac{\hat{\tau}_{im}^{-1}}{2} \left( \frac{\partial \hat{\tau}_{jm}}{\partial t} + U_k \frac{\partial \hat{\tau}_{jm}}{\partial x_k} \right) \right] u'_j, \end{aligned} \quad (19)$$

where  $\hat{\tau}_{ij}$  is the turbulent stress tensor divided by the air density, and  $\hat{\tau}_{ij}^{-1}$  is the inverse turbulent stress tensor. Both of these tensors are described in more detail in Mueller and Veron (2009a). The first term in  $a_i$  is the fading memory term such that, when discretized, the velocity has only a partial correlation with that of the previous step. The second term  $\phi_i$  is the drift term

that accounts for the inhomogeneity and nonstationarity of the flow. We further simplify Eq. (19), assuming the horizontal inhomogeneity arises from the change of coordinates due to the wavy bottom boundary (see Mueller and Veron 2009a). With these assumptions, the turbulent component of Eq. (17) in its discretized form reduces to

$$\begin{aligned} u'_i(t + \Delta t) = & u'_i(t) - (1 - R_i) \sigma_i^2 \hat{\tau}_{ik}^{-1} u'_k \\ & + (1 - R_i) T_{L_i} \Phi_i + \sqrt{1 - R_i^2} \gamma_{u_i}, \end{aligned} \quad (20)$$

where  $t$  is time, and  $\Delta t$  is the numerical time step;  $\sigma_i^2$  is the variance of the  $i$ th turbulent velocity component;  $\Phi_i$  is the simplified drift term;  $T_{L_i} = 2\sigma_i^2/C_0 \epsilon_m$  is the local Lagrangian integral time scale; and  $\gamma_{u_i}$  is an independent Gaussian variable with zero mean and unit variance.

Because drops with density greater than the air do not follow the airflow exactly due to their inertia, the evolution of air velocity surrounding a sea spray drop must be decorrelated in both time and space. We take the two heavy particle autocorrelation coefficients from Mueller and Veron (2009a) that include both the Lagrangian time scale and Eulerian length scales as

$$R_1 = \exp \left[ -\frac{\Delta t}{T_{L_1}} - \left( \frac{|s_1|}{L_{f_1}} \right)^{2/3} - \left( \frac{|s_3|}{L_{g_3}} \right)^{2/3} \right], \quad (21)$$

$$R_3 = \exp \left[ -\frac{\Delta t}{T_{L_3}} - \left( \frac{|s_3|}{L_{f_3}} \right)^{2/3} - \left( \frac{|s_1|}{L_{g_1}} \right)^{2/3} \right], \quad (22)$$

where  $\mathbf{s}$  is the separation vector between an air parcel trajectory and the heavy particle trajectory at each time step, and  $L_f$  and  $L_g$  are the longitudinal and transverse Eulerian length scales, respectively. Here,  $L_{f_i} = 2L_{g_i} = \sigma_i^3/2\epsilon_m$ . This model differentiates the direction of the separation between the air and heavy particle at each time step and decorrelates the velocity from the previous time step accordingly. Note that this autocorrelation function [Eqs. (21)–(22)] satisfies the limits: an extremely heavy particle falling through the eddies and an air element following the eddies exactly.

The turbulent deviations of the scalar fields are modeled similarly to the velocity field. For the scalar turbulent components of a fluid parcel, we consider a Langevin-type evolution:

$$d\theta' = a_\theta dt + b_{\theta u_3} d\xi_{u_3} + b_\theta d\xi_\theta, \quad (23)$$

$$dq' = a_q dt + b_{qu_3} d\xi_{u_3} + b_q d\xi_q, \quad (24)$$

where  $d\xi_{u_3}$ ,  $d\xi_\theta$ , and  $d\xi_q$  are independent Gaussian variables with zero mean and variance  $dt$ .

Although the corresponding probability distribution function may not be exact in this scalar turbulence model, the one-point correlations can still be recovered if we instead follow an approach similar to [Moissette et al. \(2001\)](#). Accordingly, the first terms in Eqs. (23) and (24) follow the form of the classical Langevin equation:

$$a_\theta = -\frac{C_\theta \epsilon_\theta \theta'}{\sigma_\theta^2} = -\frac{\theta'}{T_{L_\theta}}, \quad (25)$$

$$a_q = -\frac{C_q \epsilon_q q'}{\sigma_q^2} = -\frac{q'}{T_{L_q}}, \quad (26)$$

where  $C_\theta \approx \pi/2$  and  $C_q \approx \pi/2$  are the constants from the second-order Lagrangian structure functions of temperature and water vapor, respectively, and  $\epsilon_\theta$  and  $\epsilon_q$  are the scalar dissipation rates. The corresponding variances for the scalar turbulence are  $\sigma_\theta^2$  and  $\sigma_q^2$ . The specification of these scalar dissipation rates and integral time scales  $T_{L_\theta} = \sigma_\theta^2 / C_\theta \epsilon_\theta$  and  $T_{L_q} = \sigma_q^2 / C_q \epsilon_q$  can be found in [Mueller and Veron \(2010b\)](#). The diffusion terms  $b_\theta$  and  $b_q$ , which are similar to their velocity counterparts, are modified to ensure that the heat and water vapor fluxes, that is, the covariances, are recovered:

$$b_\theta = \sqrt{2C_\theta \epsilon_\theta \left(1 - \frac{\hat{H}_{\theta\theta}^2}{\hat{H}_{\theta\theta} \hat{\tau}_{33}}\right)}, \quad (27)$$

$$b_q = \sqrt{2C_q \epsilon_q \left(1 - \frac{\hat{M}_{q3}^2}{\hat{M}_{qq} \hat{\tau}_{33}}\right)}, \quad (28)$$

where  $\hat{H}$  and  $\hat{M}$  are, respectively, the turbulent water vapor flux divided by the density of air and the turbulent heat flux divided by the density and isobaric specific heat of air.

The Wiener process in Eqs. (23) and (24) should evolve as the second-order Lagrangian structure function of (vertical) velocity and temperature or water vapor ([Couzinet 2008](#)); but to ensure that all second-order, one-point correlations are recovered, these terms are taken to be

$$b_{\theta u_3} = \sqrt{2C_\theta \epsilon_\theta \hat{H}_{\theta 3}} / \sqrt{\hat{H}_{\theta\theta} \hat{\tau}_{33}}, \quad (29)$$

$$b_{q u_3} = \sqrt{2C_q \epsilon_q \hat{M}_{q 3}} / \sqrt{\hat{M}_{qq} \hat{\tau}_{33}}. \quad (30)$$

In discretized form, the temperature and water vapor fluctuations at each subsequent time step are

$$\begin{aligned} \theta'(t + \Delta t) = & \theta'(t)R_\theta + \sigma_\theta \sqrt{1 - R_\theta^2} \\ & \times \left( \gamma_{u_3} \hat{H}_{\theta 3} / \sqrt{\hat{H}_{\theta\theta} \hat{\tau}_{33}} + \gamma_\theta \sqrt{1 - \frac{\hat{H}_{\theta\theta}^2}{\hat{H}_{\theta\theta} \hat{\tau}_{33}}} \right), \end{aligned} \quad (31)$$

$$\begin{aligned} q'(t + \Delta t) = & q'(t)R_q + \sigma_q \sqrt{1 - R_q^2} \\ & \times \left( \gamma_{u_3} \hat{M}_{q 3} / \sqrt{\hat{M}_{qq} \hat{\tau}_{33}} + \gamma_q \sqrt{1 - \frac{\hat{M}_{q3}^2}{\hat{M}_{qq} \hat{\tau}_{33}}} \right), \end{aligned} \quad (32)$$

where  $\gamma_\theta$  and  $\gamma_q$  are independent Gaussian variables with zero mean and unit variance, and  $\gamma_{u_3}$  is the same as before, from Eq. (20).

We use the following two autocorrelation coefficients for sea spray drops that include both the Lagrangian time scale and Eulerian length scales:

$$R_\theta = \exp \left[ -\frac{\Delta t}{T_{L_\theta}} - \left( \frac{|s_1|}{L_{\theta 1}} \right)^{2/3} - \left( \frac{|s_3|}{L_{\theta 3}} \right)^{2/3} \right], \quad (33)$$

$$R_q = \exp \left[ -\frac{\Delta t}{T_{L_q}} - \left( \frac{|s_3|}{L_{q 3}} \right)^{2/3} - \left( \frac{|s_1|}{L_{q 1}} \right)^{2/3} \right], \quad (34)$$

where  $L_{\theta i} = \sigma_\theta^2 \sigma_i / 2\epsilon_\theta$  and  $L_{q i} = \sigma_q^2 \sigma_i / 2\epsilon_q$  are the Eulerian length scales for temperature and water vapor, respectively. Our model decorrelates the scalar turbulence in both time and space and satisfies both the limit of an extremely heavy particle falling through the turbulent eddies and that of an air parcel following the turbulent eddies.

### (iii) Droplet dynamics and microphysics

We now consider the response of the particle to the forcing airflow. In an unsteady airflow, the equation of motion<sup>1</sup> for a spherical particle of radius  $r$  and density  $\rho_p$  is [for the full, detailed derivation, see [Maxey and Riley \(1983\)](#)]

<sup>1</sup> Here, we neglect lift from shear and drop rotation (Saffman and Magnus effects) and second-order effects of the flow curvature (Faxen effects).

$$\begin{aligned}
 \left(\frac{4}{3}\pi r^3 \rho_p\right) \frac{d\mathbf{v}}{dt} &= \frac{1}{2}\rho C_p \pi r^2 (\mathbf{u} - \mathbf{v})|\mathbf{u} - \mathbf{v}| + \frac{4}{3}\pi r^3 \rho_p \mathbf{g} \\
 &+ \left(\frac{4}{3}\pi r^3 \rho\right) \left(\frac{d\mathbf{u}}{dt} - \mathbf{g}\right) + \frac{1}{2}\left(\frac{4}{3}\pi r^3 \rho\right) \left(\frac{d\mathbf{u}}{dt} - \frac{d\mathbf{v}}{dt}\right) \\
 &+ 6r^2 \rho \sqrt{\pi \nu} \int_0^t \left(\frac{d\mathbf{u}}{d\lambda} - \frac{d\mathbf{v}}{d\lambda}\right) \frac{d\lambda}{\sqrt{t-\lambda}},
 \end{aligned}
 \tag{35}$$

where  $C_p$  is the drag coefficient on the particle, and  $\mathbf{g}$  is the gravitational acceleration vector. As before, the total velocity vector of the air is given by  $\mathbf{u}$ , while that of the particle is denoted by  $\mathbf{v}$ . In the equation above, on the right-hand side, the first term is the steady viscous drag on the particle; the second term is the gravity term; the third term accounts forces from the fluid on the droplets and includes pressure gradient and viscous forces; the fourth term is the so-called added mass term that represents the forces from the acceleration of the surrounding fluid; and the last term is the Basset history term that accounts for past relative acceleration in an unsteady flow and can be related to the diffusion of vorticity from the accelerating drop. In practice, a cutoff time limit for the Basset history integration avoids prohibitively expensive calculation at each time step.

All the terms that are introduced from the unsteadiness of the flow, terms three to five on the right-hand side, are typically neglected in most particle dispersion models. This typical simplification is normally justified because the ratio of the particle density to the air density is large, that is,  $(\rho_p/\rho) \geq O(10^3)$ . While this simplification is valid if the temporal velocity gradients are small, it is not accurate when these gradients of either the air or the particle are large. For example, when sea spray droplets are ejected from the water surface and when particles in general fall through the near-surface boundary layer, these terms can become important. Our model solves Eq. (35) without further simplification using a fourth-order Runge–Kutta scheme at each time step.

The instantaneous drag coefficient on the particle is obtained from the steady solution (Clift and Gauvin 1970):

$$C_p = \frac{24}{\text{Re}_p} \left( 1 + 0.15 \text{Re}_p^{0.687} + \frac{0.0175 \text{Re}_p}{1 + 4.25 \times 10^4 \text{Re}_p^{-1.16}} \right),
 \tag{36}$$

where  $\text{Re}_p = 2r|\mathbf{u} - \mathbf{v}|/\nu$  is the instantaneous particle Reynolds number.

For the microphysics, the thermal and evaporation response of the droplet to its environment, we base our approach on the work of Andreas (1989), which extended the work of Pruppacher and Klett (1978) on the evolution of aqueous drops to saline sea spray droplets. He found two distinct time scales for the evolution of saline droplets subjected to constant ambient conditions. The first time scale is the adjustment time for a droplet to reach its wet bulb temperature, modified for the effects of curvature and salinity. Depending on the radius and ambient conditions, the time scale is  $O(10^{-4}-1)$  s. During this initial phase, the droplet retains almost all of its water mass. The second time scale is the time required for the droplet to lose a significant amount of its water mass and is approximately three orders of magnitude greater. Consequently, numerous models, studies, and spray-mediated flux estimates have typically taken advantage of the separation between these time scales to simplify the modeled microphysics.

We can now evaluate the evolution of a droplet size and temperature as it traverses through the turbulent marine boundary layer. In addition, the evolution of drop density and salinity can also be evaluated. Following Andreas (1989) and Edson and Fairall (1994), the temporal evolution of the radius of a saline (NaCl) water droplet in air is

$$\begin{aligned}
 \frac{dr}{dt} &= \frac{f_w D'_w M_w e_s(T_a)}{\rho_p r R T_a} \\
 &\times \left[ Q_{\text{RH}} - \frac{1}{1+\delta} \exp\left(\frac{L_v M_w}{R T_a} \frac{\delta}{1+\delta} + \Upsilon\right) \right],
 \end{aligned}
 \tag{37}$$

where

$$\Upsilon = \frac{2M_w \Gamma_p}{R T_a \rho_w r (1+\delta)} - \frac{I \Phi_s m_s (M_w/M_s)}{(4\pi r^3 \rho_p/3) - m_s}.$$

And the temporal evolution of the droplet temperature  $T_p$  is

$$\frac{d}{dt}(T_a - T_p) = \frac{-3}{r^2 \rho_p c_{ps}} [f_h k'_a (T_a - T_p) + f_w L_v D'_w (\rho q - q_p)].
 \tag{38}$$

The quantity  $Q_{\text{RH}}$  is the fractional relative humidity,  $\rho_p$  is the particle density, and  $\rho_w$  is the pure water density;  $R$  is the universal gas constant;  $M_w$  and  $M_s$  are the molecular weight of water and salt, respectively;  $e_s(T_a)$  is the saturation vapor pressure at the air temperature  $T_a$ ;  $c_{ps}$  is the specific heat of salty water;  $L_v$  is the latent heat of vaporization;  $\Gamma_p$  is the surface tension for a flat surface at the interface of the drop;  $m_s$  is the mass of salt in the droplet;  $I$  is the number of ions salt dissociates into

( $I = 2$ );  $\phi_s$  is the osmotic coefficient; and  $\delta = T_p/T_a - 1$ . The specific humidity for moist air  $q$  is modeled as described above.

The water vapor density on the droplet surface is

$$q_p = \frac{M_w e_s(T_p)}{RT_p} \exp(Y). \quad (39)$$

The modified diffusivity for water vapor  $D'_w$  and the thermal conductivity of air  $k'_a$  include noncontinuum effects and are, respectively,

$$D'_w = \epsilon \left/ \left[ \frac{r}{r + \Delta_w} + \frac{\epsilon}{r\alpha_c} \left( \frac{2\pi M_w}{RT_a} \right)^{1/2} \right] \right., \quad (40)$$

$$k'_a = k_a \left/ \left[ \frac{r}{r + \Delta_T} + \frac{k_a}{r\alpha_T \rho_{ad} c_{pd}} \left( \frac{2\pi M_a}{RT_a} \right)^{1/2} \right] \right., \quad (41)$$

where  $\epsilon$  and  $k_a$  are the molecular diffusivity for water vapor and thermal conductivity of air, respectively;  $M_a$  is the molecular weight of dry air;  $c_{pd}$  and  $\rho_{ad}$  are, respectively, the specific heat and density for dry air and with constants  $\Delta_w = 8 \times 10^{-8}$ ,  $\alpha_c = 0.036$ ,  $\Delta_T = 2.16 \times 10^{-7}$ , and  $\alpha_T = 0.7$ . Ventilation coefficients  $f_w = f_h = 1 + \sqrt{\text{Re}_p}/4$  are corrections to the heat and water vapor diffusivity for large instantaneous particle Reynolds numbers, that is,  $\text{Re}_p \gg 1$ .

## 2) MODEL CASE

After several test cases that were used to optimize droplet radii bins and wind speeds, we settled on the following comprehensive set of conditions. We ran the model for thirty initial drop radius bins ( $r_0 = 25, 30, 35, 40, 45, 50, 55, 60, 65, 70, 75, 80, 85, 90, 95, 100, 105, 115, 125, 135, 150, 170, 200, 250, 300, 500, 750, 1000, 1500,$  and  $2000 \mu\text{m}$ ) and for eight 10-m wind speeds [ $U_1(10) = 5, 10, 15, 20, 25, 30, 40,$  and  $50 \text{ m s}^{-1}$ ]. The surface values for temperature, relative humidity, salinity, and pressure were  $20^\circ\text{C}$ ,  $98\%$ ,  $34 \text{ psu}$ , and  $101325 \text{ Pa}$ , respectively. The 10-m air temperature and relative humidity were  $18^\circ\text{C}$  and  $85\%$ , respectively. We assume hydrostatic pressure, when solving for the mean 10-m pressure value.

Approximately 8000 drop trajectories were simulated for each diameter and wind speed at the lower wind speeds.<sup>2</sup> Drops are ejected in groups of 16 above the crest of the highest wave in a domain containing 500 peak wavelengths. For each group, a new realization of

the ocean surface is regenerated using a new set of random wave phases. The drops are initially randomly distributed following a uniform distribution within 3.75 cm of the horizontal location of the peak wave crest. Hereafter, for practical reasons, we also make a change of horizontal coordinates such that  $\overline{x(0)} = 0$ .

The initial height above the surface is taken to be

$$\zeta_0 = r_0 + 10\nu/u_* + z_m. \quad (42)$$

This parameterization of the initial height places the bottom of each drop at the top of the viscous layer plus the roughness length. Furthermore, the drops are assumed to be spherical, and the location of a drop at each time step is referenced to the center of the drop. In the absence of reliable data for the ejection of spume drops, we chose conservative initial conditions to estimate a lower bound. The top of the viscous layer plus the roughness length is effectively the minimum height, as turbulent transport is negligible inside the viscous layer. Although the measurements of [Veron et al. \(2007\)](#) suggest that the viscous layer disappears when breaking and airflow separation occurs, which would mean that drop ejection could effectively take place within a roughness length of the surface, some of our recent measurements ([Veron et al. 2012](#)) indicate that drops are likely to be generated when fluid sheets and filament dislocate at heights of order  $O(1-5)$  cm, but this still needs to be confirmed.

Since it is assumed that drops are ejected concurrently with surface-breaking events ([Mueller and Veron 2009c](#)), the initial velocity for all the drops was taken to be the air velocity at the bottom of the drop, which included the wave-induced velocity and the effects of airflow separation. The wave-coherent vertical velocity component that is normally determined such that the airflow follows the surface (i.e., the local, mean horizontal velocity multiplied by the wave slope, exponentially damped with height) is instead initially calculated as the local, mean horizontal velocity multiplied by the average slope from the crest to one-fourth of the peak wavelength upstream of the crest. Exponentially damped with time, this initial upward velocity relaxes back to the normal situation in which this vertical velocity component ensures that the airflow follows the surface at the surface ( $\zeta = 0$ ).

In the interim time, the net result offers a simulation of airflow separation, which presumably occurs over a breaking wave where spume drops are formed and also appears to project the mean air velocity, at least for a fraction of the downwind wavelength, at an angle that compares with the upwind wave slope ([Veron et al. 2007](#); [Kawai 1982](#); [Kawamura and Toba 1988](#); [Reul et al.](#)

<sup>2</sup>At high wind speeds, because the model is computationally expensive, we stopped runs once convergence was attained, so the final number of drops simulated for each radius bin is not uniform.

2008). Indeed, the average wave slope on the leeward side of the wave should be roughly the opposite of the slope on the upstream side of the wave. Thus, the two components, on average, should roughly simulate an airflow separation event at the beginning of the drop transport. The expression for this wave phase, coherent, vertical velocity is

$$\begin{aligned} \tilde{u}_3(x, \zeta, t) = & U_1(\zeta, x) \bar{\alpha}_0 \exp(-t/\tau_b) \\ & + U_1(\zeta, x) \sum_n \frac{\partial \eta_n(x, t)}{\partial x} \exp(-k_n \zeta) \\ & \times [1 - \exp(-t/\tau_b)], \end{aligned} \quad (43)$$

where  $\tau_b$  is the breaking wave time scale, that is, the breaking duration, assumed to be one-tenth of the peak wave period, and  $\bar{\alpha}_0$  is the average slope from the crest to one-fourth of the peak wavelength upstream of the crest. After the initial disturbance, the airflow returns to normal. Incidentally, the resulting angle of the initial drop velocity vector never exceeds, in normal wind-wave conditions, the initial angle of  $30^\circ$  relative to the horizontal, which Pattison and Belcher (1999) assumed for spume drops. Their initial angle matched the angle that the wind whips sand particles into the air from the ground (Nalpanis et al. 1993).

Together, this model case provides our best guess scenario for the spray-mediated fluxes. We note here that a second scenario for the drops' initial conditions was run; this second scenario assumed very conservative initial conditions for both the drop ejection height and velocity (at the viscous sublayer height and corresponding airspeed) and provided a natural lower bound for the spray-mediated fluxes. An additional scenario for the upper bound is unnecessary because, as shown below, our results predict lower spray-mediated fluxes than other studies in the literature that have made reasonable assumptions about the residence time and fluxes per drop. In essence, conventional wisdom provides a reasonable upper bound for this study.

### 3. Results

#### a. Mean transport

The amount of time that sea spray drops spend in the air is a limiting factor to the magnitude of the spray-mediated fluxes, but to a lesser extent for the sensible heat flux. The shorter the time that the drop resides in the air, the lower the potential for mass and latent heat transfer. Figure 1a shows the mean residence time as a function of drop initial radius  $r_0$ . In general, the smaller drops stay suspended longer than larger ones because of their relative net gravitational forces. This rule breaks

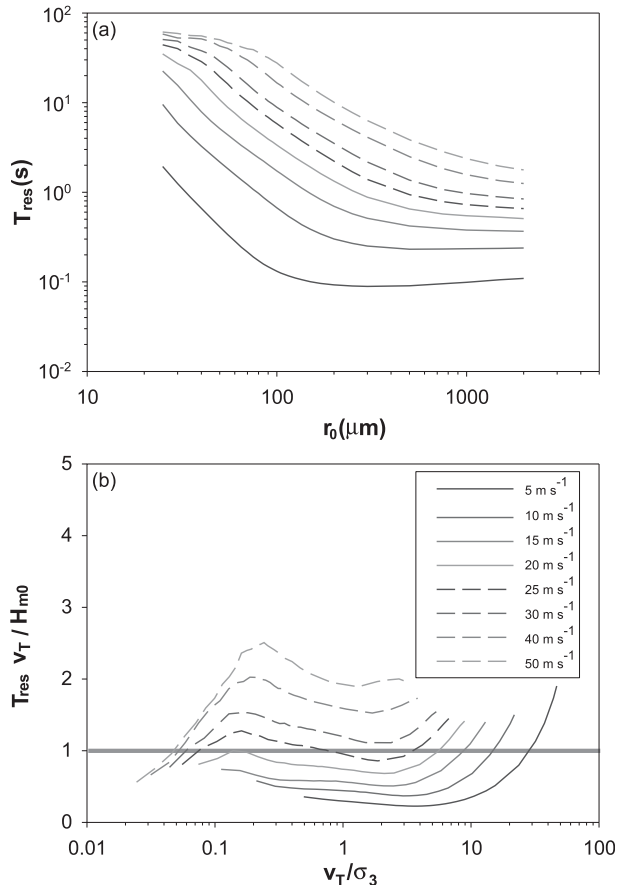


FIG. 1. (a) The mean residence time as a function of initial radius  $r_0$  for various 10-m equivalent wind speeds  $U_{10}$ . (b) The mean residence time normalized by the significant wave height  $H_{m0}$  divided by the terminal velocity  $v_T$  as a function of  $v_T$  divided by the standard deviation of the vertical air velocity fluctuations;  $U_{10}$  ranges from 5 to  $50 \text{ m s}^{-1}$ .

down at the lowest wind speeds, however, where the largest drops stay suspended slightly longer. The significant inertia of the largest drops from the initial velocity becomes relatively more influential at low wind speeds because the residence times are so brief. In fact, even the smallest drops spend less than 10 s in the air at the lowest wind speeds. At the intermediate wind speeds, the radius dependence of the residence time is similar. By the highest wind speeds, however, the residence time of the smallest drops plateaus, when the turbulent transport completely dominates, replacing the normal trade-off between gravitational settling and turbulent transport.

Figure 1b shows the residence time normalized by the time it would take a drop to fall one significant wave height, as modeled, at terminal velocity as a function of the relative gravitational settling and vertical turbulent velocity. Parameterizing the residence time of spray droplets in such a way is common practice in the community

(see, e.g., Andreas 2004). Our model appears to depart from this simple estimate by a factor ranging from 0.5 to 2. At low wind speeds, the free fall approach projects longer residence times for all drop sizes except for the very largest drops for which initial ejection velocities play a role. At wind speeds higher than  $30 \text{ m s}^{-1}$ , the settling velocity becomes irrelevant as the air turbulence dominates the drop trajectories and the residence time becomes larger than that predicted by a free fall from the significant wave height.

When the ratio of the terminal velocity and standard deviation of vertical velocity is close to 1, the time ratio is roughly constant for low and intermediate wind speeds. Nevertheless, these results suggest that residence times are not related to the significant wave height in a simple way. Droplets, depending on their size and inertia, may also fall back quickly and not far from the crest from which they were ejected (see Figs. 2 and 6 below).

We note here that the ratio of the terminal velocity to the vertical turbulent velocity  $v_T/\sigma_3$  is essentially a measure of the drops' drag versus their inertia for different wind speed conditions. When  $v_T/\sigma_3 < 1$ , drops are typically small and can be thought of as following the turbulent flow nearly passively; when  $v_T/\sigma_3 > 1$ , drops are larger and are less influenced by the ambient turbulence.<sup>3</sup>

For the intermediate and high wind speeds, all drop sizes travel at mean horizontal speeds between 60% and 90% of the 10-m wind speed, as shown in Fig. 2a. Even traveling at these speeds for a few seconds or minutes, the drops can travel long distances. While even the smallest drops travel less than 100 m at low wind speeds, by  $30 \text{ m s}^{-1}$  the smallest drops travel about a kilometer (see Fig. 2b.) At  $50 \text{ m s}^{-1}$ , even drops larger than  $100 \mu\text{m}$  travel a kilometer or more.

The horizontal transport is aided by the slower effective settling velocities. Figure 3a shows the average vertical drop velocities normalized by terminal velocity. All but the smallest drops settle slower than that predicted from terminal velocities in a still fluid. In contrast, the smallest drops can fall faster than their terminal velocities on average because they follow the airflow closely, upsetting the normal balance between gravitational settling and turbulent transport in near-exclusive favor of turbulent transport. The different size drops

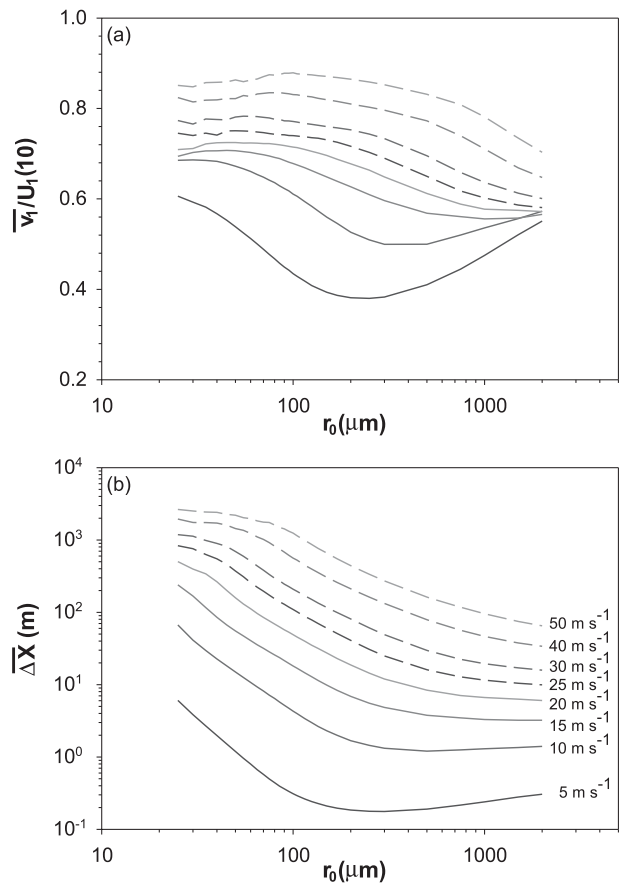


FIG. 2. (a) Mean horizontal drop velocity normalized by the 10-m wind speed as a function of initial radius. (b) Mean distance traveled as a function of initial radius.

follow the turbulent eddies differently and disperse accordingly. Figure 3b shows the average height above the wavy surface normalized by the significant wave height, as a function of initial radius. At the lower wind speeds, drops of all sizes generally reside below a significant wave height. At the high wind speeds, the smallest droplets will be, on average, transported at heights larger than the significant wave height. The different locations of drop sizes expose the drops to different conditions—wind speed, turbulent intensity, temperature, and humidity.

We now take a look at the distribution of drop locations above the surface. Figure 4 shows the histogram of the times a drop location is at a height above the surface, normalized by the mean residence time, for six initial drop radii at four wind speeds. Note that these plots illustrate the average results from the Lagrangian stochastic simulations and consequently are not weighted by any sea spray generation function. Any discontinuities in the data, such as at the top of Fig. 4d, reflect the imperfect selection of bin locations. In general, as the

<sup>3</sup>This can be thought of as the Stokes number where the time scale for the turbulence is taken as  $\tau_{\text{turb}} = \sigma_3/g$ , although the reader is reminded that the terminal velocity, taken positive downward, calculated here differs slightly from the Stokes terminal velocity [see Eq. (36)].

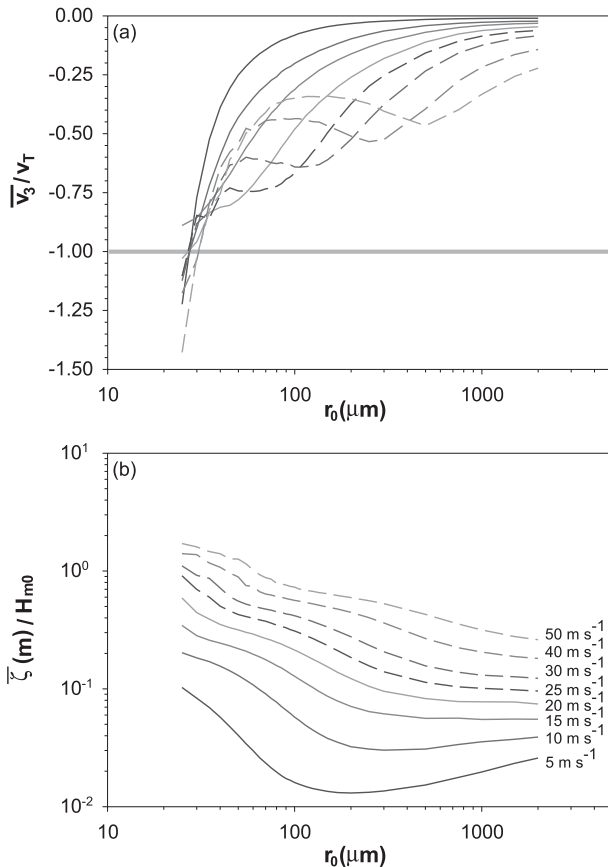


FIG. 3. (a) Mean vertical drop velocity normalized by  $v_T$  as function of initial radius. (b) Mean height above the wavy surface normalized by the significant wave height as a function of the initial radius.

initial drop size gets smaller, the drops disperse more and to greater heights; dispersion also increases with the wind speed, suggesting that the distribution of the drop location above the surface depends almost exclusively on the relative gravitational and turbulent forces.

Balancing gravitational settling and production/turbulent diffusion, Fairall et al. (2009) showed that the drop concentration above a source height is a power law of height. The upper part of the distributions (above the peak, the source height) shown in Fig. 4 compare quite well with the power-law profiles as would be expected since the Lagrangian stochastic model is essentially a sophisticated random walk, diffusion-type model. One notable exception is that the power-law profile predicts marginally higher concentration at higher altitudes. This is the result of the assumption of a constant turbulent intensity with height for the power-law model and a varying turbulent intensity with height in our model where the turbulent stress near the surface is reduced as a fraction of the total stress is supported by the surface waves. The wave field characteristics, yet somewhat

surprisingly, seem to play a lesser role for all but the weakest winds.

It should be noted here that our model, while simulating small-scale turbulence using the stochastic Lagrangian approach, lacks the ability to represent large-scale atmospheric structures, such as boundary layer rolls, which have the potential to transport a significant amount of relatively large drops [ $O(100) \mu\text{m}$  up to the height of the atmospheric boundary layer, several hundreds of meters high (Shpund et al. 2011, 2012)]. This shortcoming will limit the impact of sea spray to the near surface and could lead to greater heat and mass transfers close to the surface with much less transfer at upper levels compared to the well-mixed boundary layer in the presence of large eddies.

The maximum height above the surface is another interesting factor to consider. While the general rule is that the smaller the drop and greater the turbulent intensity, the higher the maximum height, this rule breaks down in a couple of instances, as shown in Fig. 5a. At low wind speeds, some of the largest drops reach greater heights than slightly smaller ones because the low turbulent intensity is sufficiently weak that the initial conditions and greater inertia of the largest drops transport them higher. At moderate wind speeds, the drops seem to stay within 10 m of the surface. At high wind speeds, many of the drop sizes reach heights greater than 10 m above the surface, though the subset of drops that re-enter the ocean during the simulation time never reaches, on average, heights much greater than 10 m above the surface.

Figure 5b shows the mean maximum height above the surface normalized by the significant wave height. While the significant wave height collapses the data slightly, its influence on the maximum height above the surface appears to be minimal. Up to wind speeds of  $25 \text{ m s}^{-1}$ , most of the drops stay within one significant wave height of the surface. These drops would therefore be missed by conventional fixed height measurements at sea. At high wind speeds, drops that reach a height roughly two significant wave heights above the surface seem to stay suspended for the duration of simulation. This appears to corroborate the supposition of Andreas et al. (1995) that the height of the droplet evaporation layer is nominally one significant wave height.

So far we have considered all drops whether they fall back into the ocean during the simulation or not. Now we turn our focus to the drops that fall back and impact the surface. Figure 6a shows the average height change between start and final impact. Generally the distance that the drops fall, in a fixed vertical coordinate system, increases with increasing wind speed. Such an increase corresponds with the increase in wave heights for higher

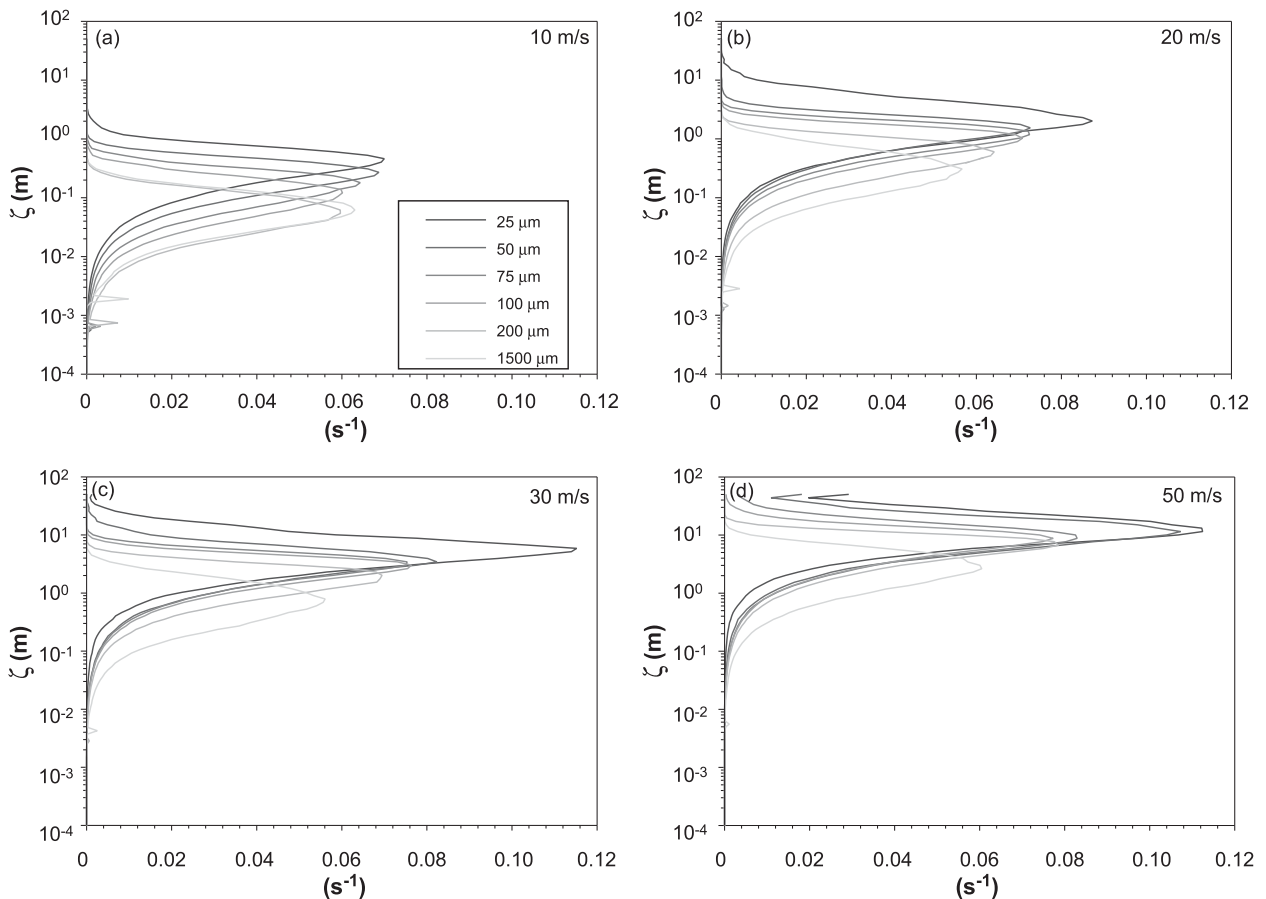


FIG. 4. Histograms of the drop heights above the surface. The distributions are normalized by the mean residence times. We show several drop radii from 25 to 1500  $\mu\text{m}$  at (a) 10, (b) 20, (c) 30, and (d) 50  $\text{m s}^{-1}$  10-m wind speeds.

wind seas. Figure 6b shows the change in height normalized by the significant wave height as a function of the ratio of terminal velocity and vertical turbulent intensity. Therein, the data collapse somewhat, especially for the smaller drops that have less gravitational settling relative to the vertical turbulent intensity. Those drops fall roughly 65%–70% of the significant wave height. The larger drops settle faster and are unable to accelerate completely to the airflow; consequently, they tend to reenter the ocean by hitting the top of a subsequent wave or by getting caught from behind by a previous wave. In other words, drops that fall less than half a significant wave height are reentering the ocean at the upper regions of the wave field.

#### b. Mean drop properties upon impact

As the drops traverse the marine boundary layer, they exchange momentum, heat, and mass. The properties of the drops upon falling back into the ocean are of particular interest because they offer insight into the net spray-mediated fluxes.

During their ascent, drops accelerate to the local wind velocity, and as they settle downward they decelerate to the local wind velocity. The final velocity is a function of the highest height attained, the drop inertia, and the gradient of the mean velocity field. As Fig. 7a shows, the horizontal velocity upon impact can be about 75% of the 10-m wind speed for the largest drops at high winds. At the high wind speeds, the largest drops stay suspended long enough to accelerate fully to the airflow mean velocity, while also settling fast enough to retain most of the peak speed before impact. At low and moderate wind speeds, the balance between momentum and gravitational settling becomes apparent. As they fall back through the boundary layer, the small drops lose much of the speed they had initially gained. The larger drops not only fall back faster but also hold their peak speed longer.

Figure 7b shows the mean vertical velocity upon impact as a fraction of the terminal velocity. Drops with initial radii greater than about 50  $\mu\text{m}$  impact the surface at velocities less than their corresponding terminal velocities.

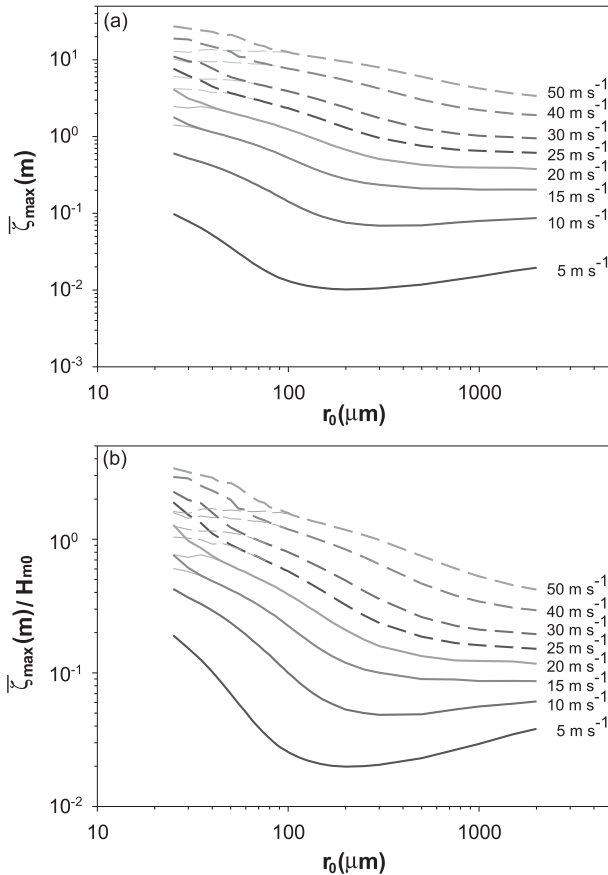


FIG. 5. (a) Mean maximum height above the wavy surface for all drops and the subset of drops that fall back into the ocean during the simulation time (thin lines) as a function of radius. (b) The mean maximum heights normalized by the significant wave height as a function of the radius.

The smaller drops can impact the surface at velocities multiple times their terminal velocity as the turbulent airflow slams them back toward the ocean. The effect of these significant drop impacts warrants further attention, but it is outside the scope of this current study.

So far we have only considered the transport and momentum transfer. Here, we consider the thermal and mass evolution of the drops. The temperature of the drop upon impact is another important variable that can be used to estimate the spray-mediated sensible heat flux. Figure 8 shows the temperature upon reentry in the ocean of 2000 water droplets of 100- $\mu\text{m}$  initial radius, for each wind speed of 5, 10, 20, 30, and 40  $\text{m s}^{-1}$ , and as a function of the time of impact. The solid black line is the temperature evolution time series for a 100- $\mu\text{m}$  radius droplet, with an initial temperature of  $T_p = 20^\circ\text{C}$ , in atmospheric condition set to exactly  $\Theta_{10} = 18^\circ\text{C}$  and relative humidity to 85% (i.e., the microphysical model alone under steady 10-m conditions).

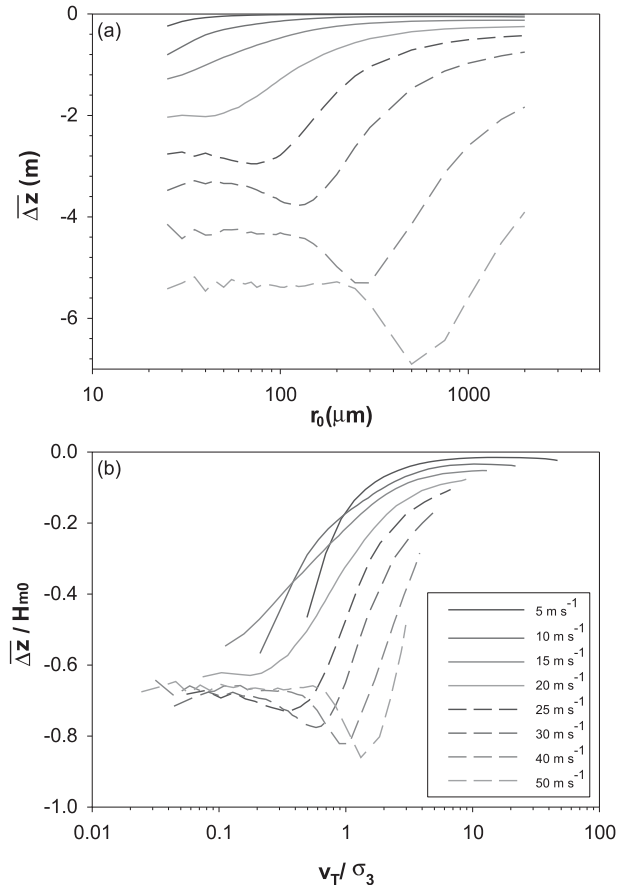


FIG. 6. (a) The mean vertical difference between the initial location of the drop and the location of drop reentry into the ocean as a function of the radius. (b) The mean vertical distance normalized by the significant wave height as a function of terminal velocity divided by the standard deviation of the vertical air velocity fluctuations.

First, we note that the particles that do remain suspended for some time (one example is shown with the thin gray line) reach a temperature that is close to that predicted by the microphysical model. The slight difference arises from the fact that the particles are exposed to conditions that are not exactly equivalent to 10-m conditions. In fact, at low wind speeds, the particles stay suspended for a short amount of time and never get exposed to 10-m atmospheric conditions.

At higher wind speeds, the drops do reach temperature nearly equivalent to that predicted by the microphysical model, but they appear to reheat prior to reentry, leading to overall impact temperatures that are significantly higher than those predicted with the microphysical model alone. Indeed, Fig. 8 shows that in the conditions chosen, the impact temperature of these 100- $\mu\text{m}$  drops, at wind speeds higher than 20  $\text{m s}^{-1}$ , is approximately  $1.5^\circ\text{C}$  warmer than expected from the steady

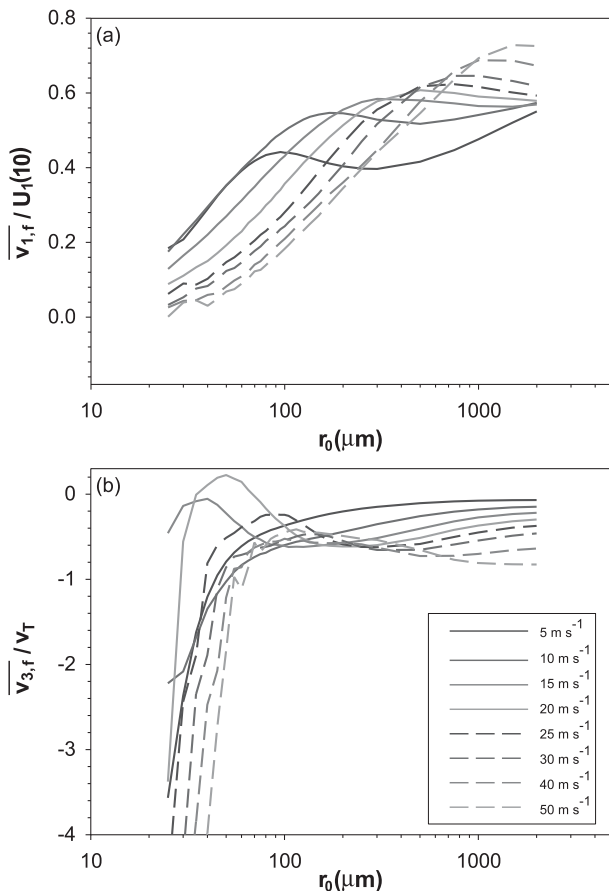


FIG. 7. (a) The mean horizontal drop velocity at impact normalized by 10-m wind speed as a function of the initial radius. (b) Mean vertical drop velocity on impact normalized by terminal velocity as a function of the radius.

microphysics. This is similar to the drop momentum exchange, whereby droplets with low inertia decelerate significantly before impact while they traverse the lower part of the boundary layer. The small spray droplets simultaneously traverse temperature and humidity boundary layers and since their sensible heat time scale (thermal inertia) is so short, they essentially reheat before impact. We additionally note from further analysis not presented here that the rewarming of the droplet before impact is largely due to the local ambient humidity (Mueller and Veron 2010b). This rewarming tendency suggests that the sensible heat flux from sea spray droplets may be lower than previously thought.

As Fig. 9a shows, the temperature change, like the momentum case, depends on two factors: thermal “inertia” and peak temperature change. At low wind speeds, the larger drops do not stay suspended long enough to reach their quasi-equilibrium, evaporating drop temperature. As the wind speed increases, more drops are able to reach their quasi-equilibrium

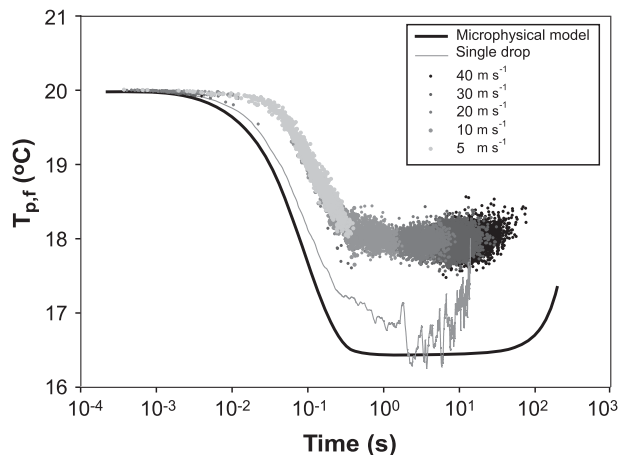


FIG. 8. Temperature upon reentry  $T_{pf}$  of 2000 droplets of radius  $100\ \mu\text{m}$  for various 10-m wind speeds. The gray line is a time series of a single droplet temperature during its flight above the wave field. Ambient conditions are a sea temperature of  $20^{\circ}\text{C}$ , salinity of 34 psu, air temperature of  $18^{\circ}\text{C}$  and 85% relative humidity. The thick black line is the prediction from the microphysical model alone using these 10-m ambient conditions.

temperature. Although the smallest drops spend enough time to reach their peak temperature change, a portion of the change is lost as they fall back because they have little thermal inertia. The data collapse when the temperature change is normalized with the temperature change predicted when holding the conditions around a drop constant as the average conditions found at one-fifth of the mean height above the surface for the length of the mean residence time. As shown in Fig. 9b, this ratio of temperature changes is roughly 1 around the ratio of terminal velocity and vertical turbulent intensity of 1. As  $v_T/\sigma_3$  increases and decreases, the ratio of temperature changes falls rapidly. Again, this means that small droplets will exchange heat as quickly before reentering the ocean, while large drops will lack sufficient time to exchange significant amounts of heat during their flight time. Except for the lowest wind speed of  $5\ \text{m s}^{-1}$  (and perhaps and  $10\ \text{m s}^{-1}$ ), this result is nearly independent of wind speed. The imperfect collapse of the data stems from the fact that the normalization with  $v_T/\sigma_3$  accounts for the inertial effects only, but does not account for the sensible heat time scales. Nevertheless, Fig. 9b indicates that the inertial effects and the dynamics of the drops play a dominant role on the net heat exchanges.

The radius and corresponding mass of the drop are also important variables that can be used to estimate the spray-mediated mass and latent heat fluxes. While the sensible heat flux time scale is quite short, the corresponding time scale for the latent heat flux tends to be significantly longer (see Andreas 1990). As Fig. 10a

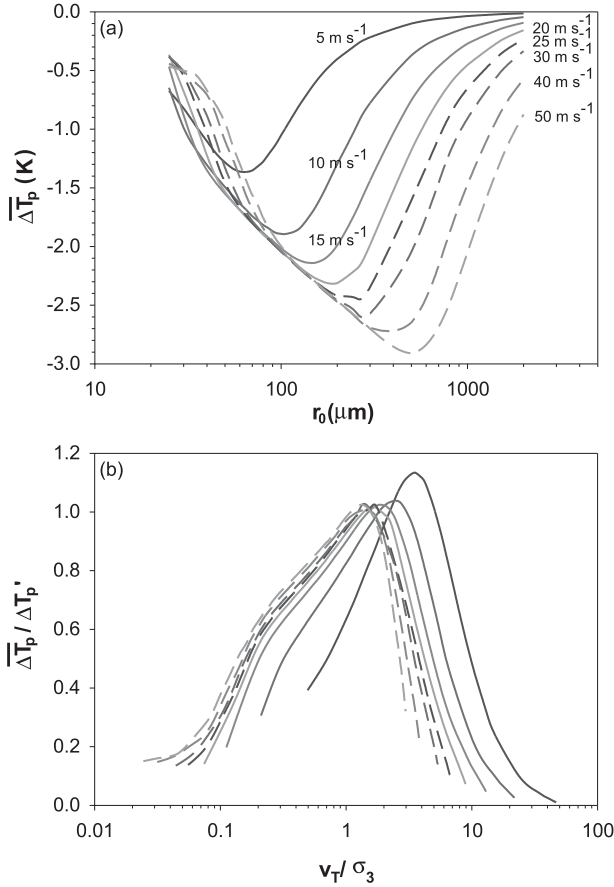


FIG. 9. (a) The mean difference between the initial temperature of the drop and final temperature upon reentry into the ocean as a function of the radius. (b) The mean temperature change normalized by the steady-state temperature evolution at one-fifth of the average height above the surface as a function of terminal velocity divided by the standard deviation of the vertical air velocity fluctuations.

shows, few of the drop sizes stay suspended long enough at low wind speeds to exchange a significant amount of water mass. As the wind forcing increases, larger and larger drops are suspended long enough to exchange a significant amount of water mass. Even at the highest wind speeds, however, the largest drops do not exchange a significant percentage of their water mass. This is due to their relatively long evaporation time scales and their relatively short residence times.

Like the temperature change case, the drop mass data collapse if we normalize the final mass upon impact with the final mass predicted when holding the conditions around a drop constant as the average conditions found at one-fifth of the mean height above the surface for the length of the mean residence time. As Fig. 10b shows, the drops with terminal velocities roughly equal to or greater than the vertical turbulent intensity evolve

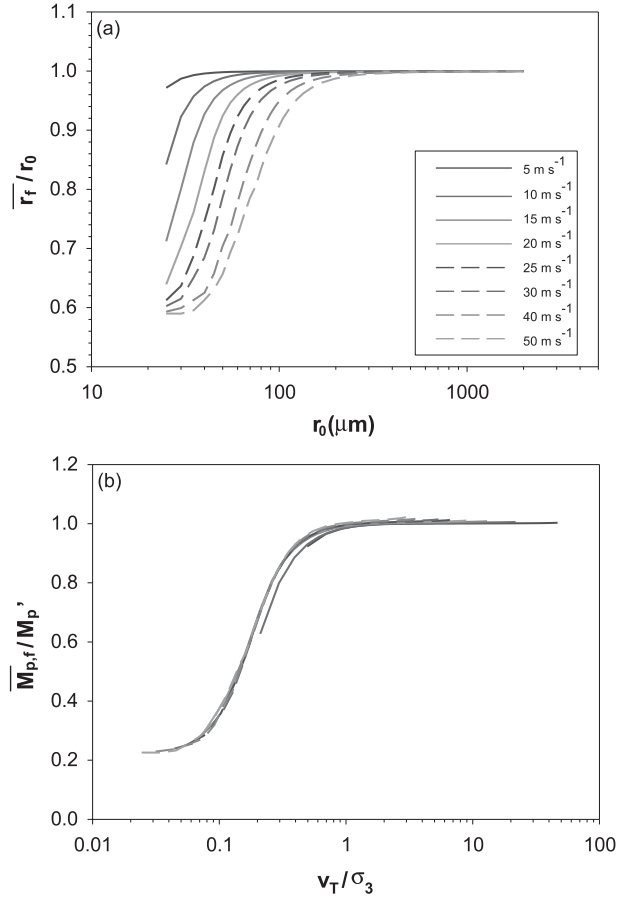


FIG. 10. (a) The mean ratio of the final radius of the drop upon reentry into the ocean and the initial radius as a function of the radius. (b) The mean final drop mass upon reentry normalized by the steady-state mass evolution at one-fifth of the average height above the surface as a function of terminal velocity divided by the standard deviation of the vertical air velocity fluctuations.

nearly identically with the steady-state evolution. The final mass decreases relative to the predicted steady-state final mass as the drops get smaller and the gravitation settling becomes less important relative to the turbulent intensity.

### c. Mean momentum and heat exchanges

For each initial drop radius  $r_0$ , the exchanges of momentum and sensible and latent heat can be expressed as

$$\Delta \tau_{\text{sp}}(r_0) = \frac{4}{3} \pi (\overline{\rho_{p,f} v_{1,f} r_f^3} - \rho_{p,0} v_{1,0} r_0^3), \quad (44)$$

$$\Delta H_{\text{sp}}(r_0) = \frac{4}{3} \pi (\overline{\rho_{p,f} c_{\text{ps},f} T_{p,f} r_f^3} - \rho_{p,0} c_{\text{ps},0} T_{p,0} r_0^3), \quad (45)$$

$$\Delta E_{\text{sp}}(r_0) = \frac{4}{3} \pi (\overline{\rho_{p,f} L_{v,f} r_f^3} - \rho_{p,0} L_{v,0} r_0^3), \quad (46)$$

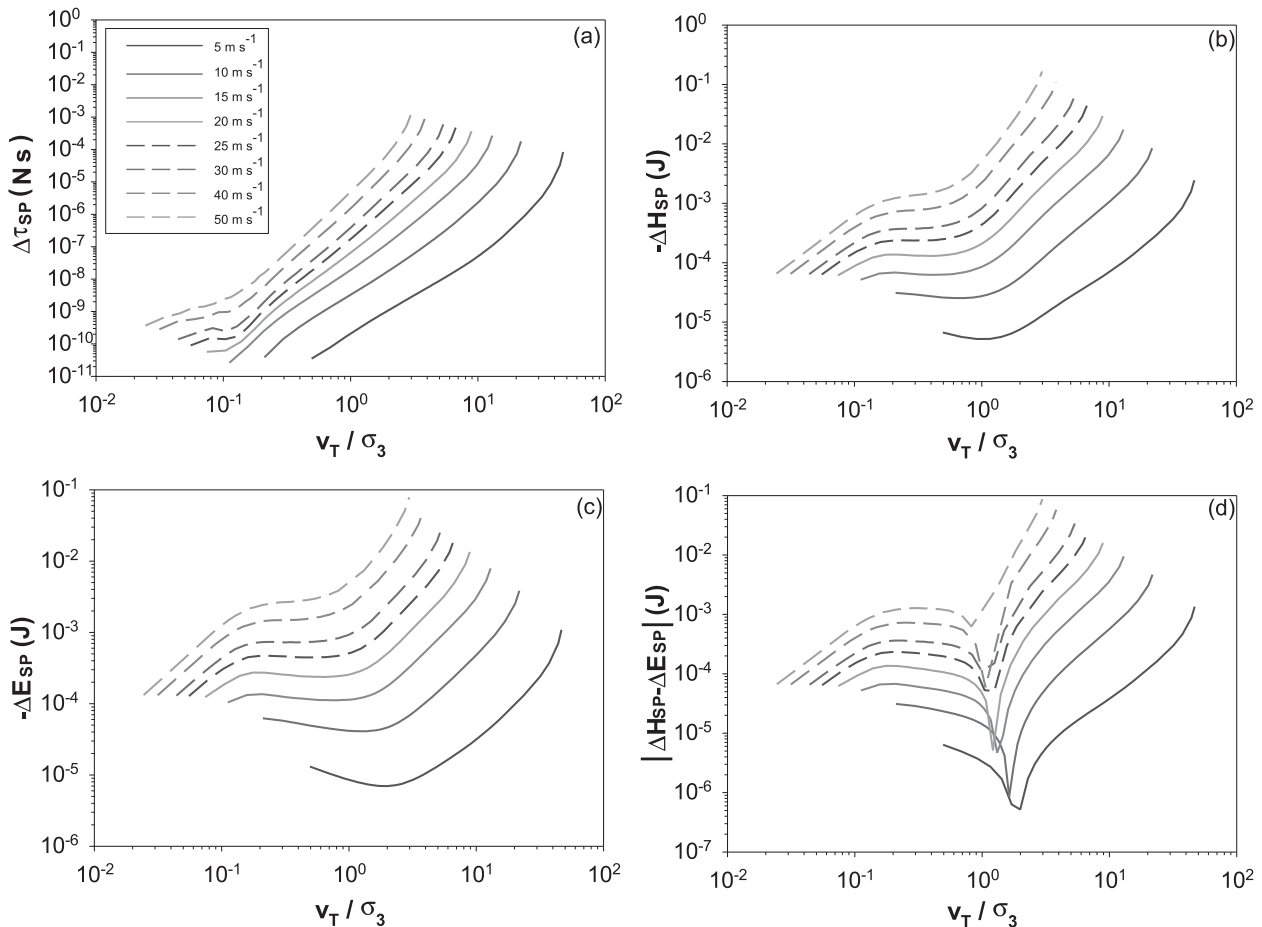


FIG. 11. The mean spray-mediated (a) momentum exchange, (b) negative sensible heat exchange, (c) negative latent heat exchange, and (d) magnitude of the net sensible heat exchange as a function of terminal velocity divided by the standard deviation of the vertical air velocity fluctuations.

where the subscripts  $f$  and  $0$  are the final and initial values, respectively. Note that these are mean exchanges on a per drop basis with units of momentum (N s) and thermal energy (J), respectively. They are not yet scaled by a sea spray generation function in order to obtain the corresponding spray momentum and heat fluxes. In Part II, the total spray-mediated fluxes, estimated using two different generation functions, will be explored.

Larger drops not only have the potential to exchange more momentum, heat, and mass, but do, in fact, exchange more on a per droplet basis. Figure 11 shows the momentum, sensible heat, latent heat, and net sensible heat exchanges for each droplet initial radius. For all exchanges, including the latent heat, the magnitudes increase with initial radius. The spray-mediated momentum exchange, shown in Fig. 11a, increases steadily with drop size because the Stokes time scale is relatively short and the mass of a drop increases with the radius to the power of three. The spray-mediated latent heat exchange shown in Fig. 11c, plateaus in the range, roughly 0.2–0.8,

of the ratio between terminal velocity and turbulent velocity fluctuations. This is the range in which the drops get transported significantly by the turbulent eddies. As the drops get smaller in this range, they stay suspended longer and contribute similar amounts to the latent heat exchanges. The spray-mediated sensible heat exchanges, shown in Fig. 11b, follow behavior somewhere in between the momentum and latent heat cases. This is most likely due to the effect of evaporation on droplet temperature, while the thermal time scale is on a similar order to the Stokes time scale.

The magnitude of the net sensible heat exchange, sensible minus latent, is shown in Fig. 11d. The positive values, or when the magnitude of the latent heat exchange is greater than the sensible heat exchange, occur with the smaller drops, left of the “kinks.” The negative values, or when the magnitude of the sensible heat exchange is greater than the latent heat exchange, correspond to the larger drops, right of the kinks. This transition occurs roughly when the terminal velocity is

between 1 to 2 times the vertical turbulent velocity. Intuitively, only the smaller lighter drops stay suspended long enough to exchange more latent heat than sensible heat. Because the small and large drops make significant contributions of opposite signs to the net sensible heat exchange on a per drop basis, these results suggest that the total spray-mediated fluxes could be rather sensitive to the source drop distribution.

#### 4. Discussion and conclusions

In this study, we have found that the mean residence time and exchanges per drop differ from previous studies. Instead of assuming the residence time is the time a drop takes to reach the surface, falling at terminal velocity when starting at an initial height of half a significant wave height, our model initializes the drops above the crest of propagating surface waves and calculates the average statistics of the turbulent transport. As a result, our model predicts residence times without a clear relationship with the significant wave height.

Drops that remain close to the surface never experience or “feel” conditions found at heights that are meters above the surface, a common assumption in previous studies. The drops that never get transported vertically evolve according to near-surface conditions that are quite different from those meters above the surface. Moreover, while some smaller drops are transported closer to 10 m and, in turn, evolve in an environment closer to the 10-m conditions, these smaller drops tend to respond quickly to near-surface conditions during their descent back into the ocean. Thus, when considering the instantaneous evolution of the drops, the magnitude of the fluxes would be comparatively lower even if the residence times were identical to those in previous studies.

There are notable differences in the features among the various drop sizes. Only drops with terminal velocities less than the vertical turbulent fluctuation exchange a significant portion of their mass with the atmosphere. As the wind speed and corresponding vertical turbulent intensity increase, larger drops lose a higher percentage of their mass to evaporation. Nevertheless, the sign of the net sensible heat exchange changes between small and large drops for all wind speeds considered here. Consequently, these results suggest that the net sensible heat flux is sensitive to the shape of the drop distribution in addition to the magnitude of the sea spray generation function. It is also important to note that we only considered one ambient relative humidity here. Previous studies (e.g., Innocentini and Gonçalves 2010; Shpund et al. 2012) have found that the magnitude of the spray-mediated heat exchanges depends strongly on the relative

humidity. Further exploration of such sensitivities to various ambient conditions will be an important component for future research.

The companion paper to this one (Part II) considers two distinct drop distributions to estimate the spray-mediated fluxes. One of the sea spray generation functions has significantly more of the larger drops than the other one. Combined with the per drop fluxes presented here, these two functions lead to drastically different fluxes and behavior, especially when the atmospheric feedback on both the interfacial and spray-mediated fluxes are considered.

*Acknowledgments.* We thank Ed Andreas, Kristina Katsaros, and an anonymous reviewer for comments that have helped improve the final version of this paper. This research was supported by Grants OCE-0850663 and OCE-0748767 from the National Science Foundation (NSF) and Grant N00014-05-1-0609 from the Office of Naval Research (ONR).

#### REFERENCES

- Andreas, E. L., 1989: Thermal and size evolution of sea spray droplets. CRREL Rep. 89-11, 47 pp.
- , 1990: Time constants for the evolution of sea spray droplets. *Tellus*, **42B**, 481–497, doi:10.1034/j.1600-0889.1990.t01-3-00007.x.
- , 2004: Spray stress revisited. *J. Phys. Oceanogr.*, **34**, 1429–1440, doi:10.1175/1520-0485(2004)034<1429:SSR>2.0.CO;2.
- , 2011: Fallacies of the enthalpy transfer coefficient over the ocean in high winds. *J. Atmos. Sci.*, **68**, 1435–1445, doi:10.1175/2011JAS3714.1.
- , J. B. Edson, E. C. Monahan, M. P. Rouault, and S. D. Smith, 1995: The spray contribution to net evaporation from the sea: A review of recent progress. *Bound.-Layer Meteor.*, **72**, 3–52, doi:10.1007/BF00712389.
- Brocchini, M., and D. H. Peregrine, 2001: The dynamics of strong turbulence at free surfaces. Part 1. Description. *J. Fluid Mech.*, **449**, 225–254, doi:10.1017/S0022112001006012.
- Clift, R., and W. H. Gauvin, 1970: The motion of particles in turbulent gas streams. *Proc. Chemeca*, **70**, 14–28.
- Couzinet, A., 2008: Approche pdf jointe fluide-particule pour la modélisation des écoulements turbulents diphasiques anisothermes. Ph.D. dissertation, L’Institut National Polytechnique de Toulouse, 185 pp.
- DeCosmo, J., K. B. Katsaros, S. D. Smith, R. J. Anderson, W. A. Oost, K. Bumke, and H. Chadwick, 1996: Air-sea exchange of water vapor and sensible heat: The Humidity Exchange over the Sea (HEXOS) results. *J. Geophys. Res.*, **101**, 12 001–12 016, doi:10.1029/95JC03796.
- Drennan, W. M., J. A. Zhang, J. R. French, C. McCormick, and P. G. Black, 2007: Turbulent fluxes in the hurricane boundary layer. Part II: Latent heat flux. *J. Atmos. Sci.*, **64**, 1103–1115, doi:10.1175/JAS3889.1.
- Edson, J. B., and C. W. Fairall, 1994: Spray droplet modeling. 1. Lagrangian model simulation of the turbulent transport of evaporating droplets. *J. Geophys. Res.*, **99**, 25 295–25 311, doi:10.1029/94JC01883.

- , S. Anquetin, P. G. Mestayer, and J. F. Sini, 1996: Spray droplet modeling: 2. An interactive Eulerian-Lagrangian model of evaporating spray droplets. *J. Geophys. Res.*, **101**, 1279–1293, doi:10.1029/95JC03280.
- Elfouhaily, T., B. Chapron, K. Katsaros, and D. Vandemark, 1997: A unified directional spectrum for long and short wind-driven waves. *J. Geophys. Res.*, **102**, 15 781–15 796, doi:10.1029/97JC00467.
- Fairall, C. W., E. F. Bradley, J. S. Godfrey, G. A. Wick, J. B. Edson, and G. S. Young, 1996a: Cool-skin and warm-layer effects on sea surface temperature. *J. Geophys. Res.*, **101**, 1295–1308, doi:10.1029/95JC03190.
- , A. A. Grachev, A. J. Bedard, and R. T. Nishiyama, 1996b: Wind, wave, stress, and surface roughness relationships from turbulence measurements made on R/P flip in the scope experiment. NOAA Tech. Memo. ERL ETL-268, 37 pp.
- , A. B. White, J. B. Edson, and J. E. Hare, 1997: Integrated shipboard measurements of the marine boundary layer. *J. Atmos. Oceanic Technol.*, **14**, 338–359, doi:10.1175/1520-0426(1997)014<0338:ISMOTM>2.0.CO;2.
- , E. F. Bradley, J. E. Hare, A. A. Grachev, and J. B. Edson, 2003: Bulk parameterization of air–sea fluxes: Updates and verification for the COARE algorithm. *J. Climate*, **16**, 571–591, doi:10.1175/1520-0442(2003)016<0571:BPOASF>2.0.CO;2.
- , M. L. Banner, W. L. Peirson, W. Asher, and R. P. Morison, 2009: Investigation of the physical scaling of sea spray spume droplet production. *J. Geophys. Res.*, **114**, C10001, doi:10.1029/2008JC004918.
- Innocentini, V., and I. A. Gonçalves, 2010: The impact of spume droplets and wave stress parameterizations on simulated near-surface maritime wind and temperature. *J. Phys. Oceanogr.*, **40**, 1373–1389, doi:10.1175/2010JPO4349.1.
- Kawai, S., 1982: Structure of air flow separation over wind wave crests. *Bound.-Layer Meteor.*, **23**, 503–521, doi:10.1007/BF00116275.
- Kawamura, H., and Y. Toba, 1988: Ordered motion in the turbulent boundary layer over wind waves. *J. Fluid Mech.*, **197**, 105–138, doi:10.1017/S0022112088003192.
- Lewis, E. R., and S. E. Schwartz, 2004: *Sea Salt Aerosol Production: Mechanisms, Methods, Measurements, and Models*. *Geophys. Monogr.*, Vol. 152, Amer. Geophys. Union, 413 pp., doi:10.1029/GM152.
- Liu, W. T., K. B. Katsaros, and J. A. Businger, 1979: Bulk parameterization of air–sea exchanges of heat and water-vapor including the molecular constraints at the interface. *J. Atmos. Sci.*, **36**, 1722–1735, doi:10.1175/1520-0469(1979)036<1722:BPOASE>2.0.CO;2.
- Mastenbroek, C., V. K. Makin, M. H. Garat, and J. P. Giovanangeli, 1996: Experimental evidence of the rapid distortion of turbulence in the air flow over water waves. *J. Fluid Mech.*, **318**, 273–302, doi:10.1017/S0022112096007124.
- Maxey, M. R., and J. J. Riley, 1983: Equation of motion for a small rigid sphere in a nonuniform flow. *Phys. Fluids*, **26**, 883–889, doi:10.1063/1.864230.
- Meirink, J., 2002: The role of wind-waves and sea spray on air–sea interaction. Ph.D. dissertation, Technische Universiteit Delft, 161 pp.
- Moissette, S., B. Oesterlé, and P. Boulet, 2001: Temperature fluctuations of discrete particles in a homogenous turbulent flow: A Lagrangian model. *Int. J. Heat Fluid Flow*, **22**, 220–226, doi:10.1016/S0142-727X(01)00083-2.
- Mueller, J. A., and F. Veron, 2009a: A Lagrangian stochastic model for heavy particle dispersion in the atmospheric marine boundary layer. *Bound.-Layer Meteor.*, **130**, 229–247, doi:10.1007/s10546-008-9340-8.
- , and —, 2009b: Nonlinear formulation of the bulk surface stress over breaking waves: Feedback mechanisms from air–flow separation. *Bound.-Layer Meteor.*, **130**, 117–134, doi:10.1007/s10546-008-9334-6.
- , and —, 2009c: A sea state-dependent spume generation function. *J. Phys. Oceanogr.*, **39**, 2363–2372, doi:10.1175/2009JPO4113.1.
- , and —, 2010a: Bulk formulation of the heat and water vapor fluxes at the air–sea interface, including nonmolecular contributions. *J. Atmos. Sci.*, **67**, 234–247, doi:10.1175/2009JAS3061.1.
- , and —, 2010b: A Lagrangian stochastic model for sea-spray evaporation in the atmospheric marine boundary layer. *Bound.-Layer Meteor.*, **137**, 135–152, doi:10.1007/s10546-010-9520-1.
- , and —, 2014: Impact of sea spray on air–sea fluxes. Part II: Feedback effects. *J. Phys. Oceanogr.*, in press.
- Nalpanis, P., J. C. R. Hunt, and C. F. Barret, 1993: Saltating particles over flat beds. *J. Fluid Mech.*, **251**, 661–685, doi:10.1017/S0022112093003568.
- Pattison, M. J., and S. E. Belcher, 1999: Production rates of sea-spray droplets. *J. Geophys. Res.*, **104**, 18 397–18 407, doi:10.1029/1999JC900090.
- Pruppacher, H. R., and J. D. Klett, 1978: *Microphysics of Clouds and Precipitation*. D. Riedel, 714 pp.
- Reul, N., H. Branger, and J.-P. Giovanangeli, 2008: Air flow structure over short-gravity breaking water waves. *Bound.-Layer Meteor.*, **126**, 477–505, doi:10.1007/s10546-007-9240-3.
- Shpund, J., M. Pinsky, and A. Khain, 2011: Microphysical structure of the marine boundary layer under strong wind and spray formation as seen from simulations using a 2D explicit microphysical model. Part I: The impact of large eddies. *J. Atmos. Sci.*, **68**, 2366–2384, doi:10.1175/2011JAS3652.1.
- , J. A. Zhang, M. Pinsky, and A. Khain, 2012: Microphysical structure of the marine boundary layer under strong wind and spray formation as seen from simulations using a 2D explicit microphysical model. Part II: The role of sea spray. *J. Atmos. Sci.*, **69**, 3501–3514, doi:10.1175/JAS-D-11-0281.1.
- Sullivan, P. P., J. C. McWilliams, and C. Moeng, 2000: Simulation of turbulent flow over idealized water waves. *J. Fluid Mech.*, **404**, 47–85, doi:10.1017/S0022112099006965.
- Thomson, D. J., 1987: Criteria for the selection of stochastic models of particle trajectories in turbulent flows. *J. Fluid Mech.*, **180**, 529–556, doi:10.1017/S0022112087001940.
- Van Driest, E. R., 1956: On turbulent flow near a wall. *J. Aeronaut. Sci.*, **23**, 1007–1011, doi:10.2514/8.3713.
- Van Eijk, A. M. J., B. S. Tranchant, and P. G. Mestayer, 2001: Seacluse: Numerical simulation of evaporating sea spray droplets. *J. Geophys. Res.*, **106**, 2573–2588, doi:10.1029/2000JC000377.
- Veron, F., G. Saxena, and S. K. Misra, 2007: Measurements of the viscous tangential stress in the airflow above wind waves. *Geophys. Res. Lett.*, **34**, L19603, doi:10.1029/2007GL031242.
- , C. Hopkins, E. Harrison, and J. Mueller, 2012: Sea spray spume droplet production in high wind speeds. *Geophys. Res. Lett.*, **39**, L16602, doi:10.1029/2012GL052603.
- Wilson, J. D., and B. L. Sawford, 1996: Review of Lagrangian stochastic models for trajectories in the turbulent atmosphere. *Bound.-Layer Meteor.*, **78**, 191–210, doi:10.1007/BF00122492.
- Zhang, J. A., P. G. Black, J. R. French, and W. M. Drennan, 2008: First direct measurements of enthalpy flux in the hurricane boundary layer: The CBLAST results. *Geophys. Res. Lett.*, **35**, L14813, doi:10.1029/2008GL034374.